

CHAPTER 3

Data Preparation and Seismic-to-Well Tie Results

Four appraisal wells (Wells A, B, C and D) were available as input to this pre-stack geostatistical inversion study, and the geophysical log data consisted of compressional velocity (V_p), shear velocity (V_s), and bulk density (Rho). Three different types of software were used in this part of the study: RokDoc (for well conditioning), MATLAB (for shear velocity prediction), and Jason (for seismic-to-well tie and geostatistical inversion).

3.1 Well-Log Data Conditioning

In general, the raw measured log data were of good to moderate quality. However, the data quality appear to be affected by borehole conditions, different borehole sizes, and missing sections. Therefore, well-log data QC and conditioning were required to improve quality and consistency of the log data. The well-log conditioning applied in the study included bad-data removal and depth-shift correction.

Anomalous log values were observed at the starting depth of measured logs such as compressional velocity (V_p), shear velocity (V_s), and density (Rho) in some wells, and mostly related to the cementation around casing points. Moreover, poor coupling between tool and borehole could create abnormal values in the log measurements. Such values were easily identified in cross-plots of well log data as they deviated from the normal shale and sand trends. Figures 3.1 and 3.2 show the original measured logs and edited logs for all input wells. After correction, unrealistic high or low values were removed and spiky data within small intervals were replaced by interpolated log values. A cross-plot of V_p and Rho was used for final QC of the well-log editing (see Figures 3.3 and 3.4). These cross-plots demonstrate how the edited log data follow the general trends, and deviating data points are removed.

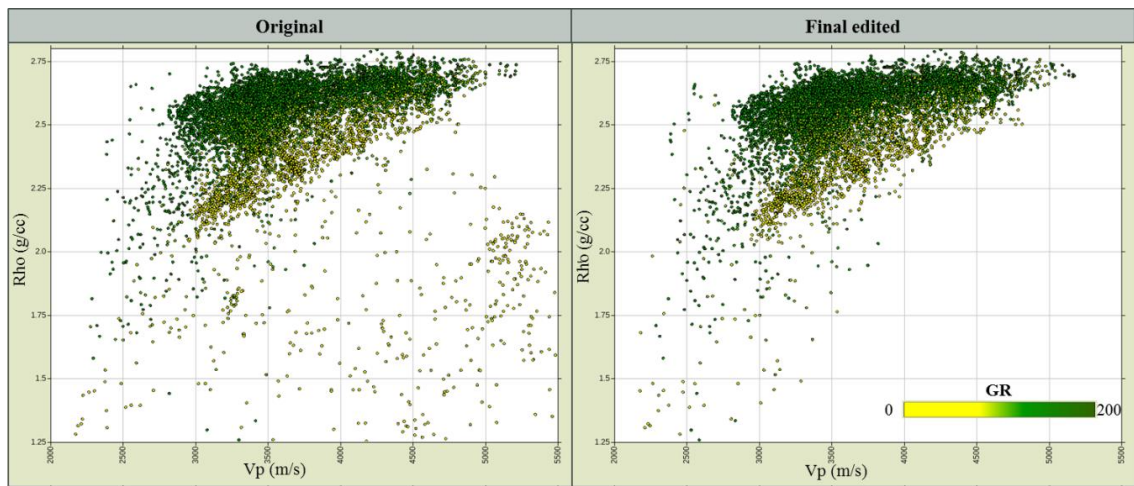


Figure 3.3 Vp vs. density (Rho) cross-plot for Well-B, original logs (left) and final logs after editing (right).

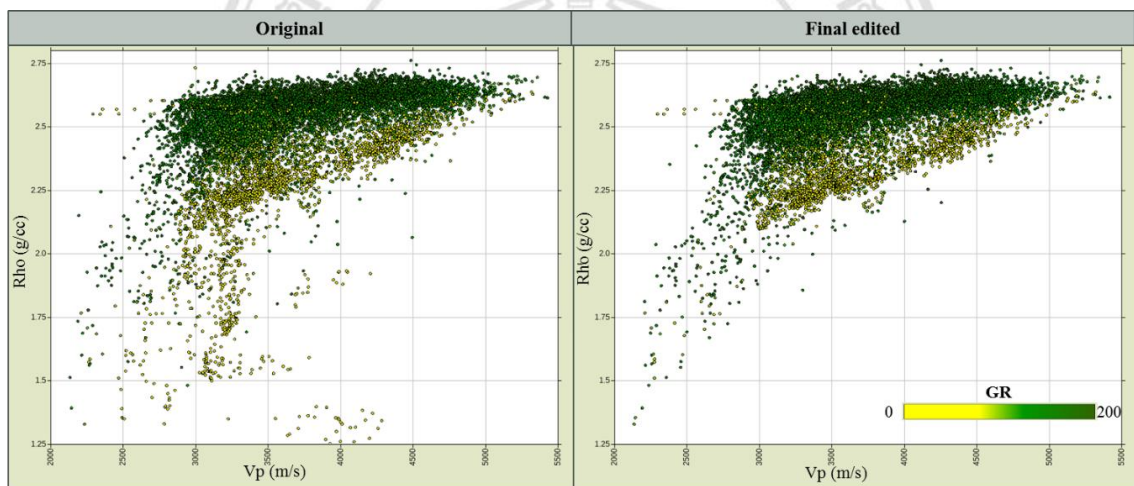


Figure 3.4 Vp vs. density (Rho) cross-plot for Well-C, original logs (left) and final logs after editing (right).

In addition, some depth shifts were observed when comparing Vp and Vs logs. Depth shifts of measured log data could occur in wells when the data was acquired by several logging runs to account for different borehole sizes. Cross-plot analysis showed that the data followed general trends and was less scattered after correcting for depth shifts (see Figures 3.5 and 3.6).

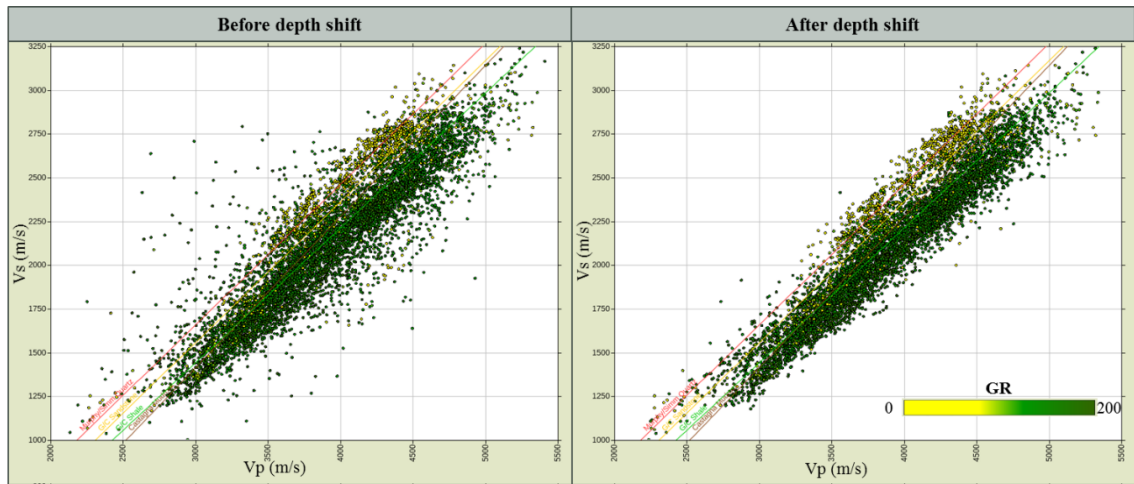


Figure 3.5 Vp vs. Vs cross-plot for Well-B, before depth shift (left) and after depth shift (right).

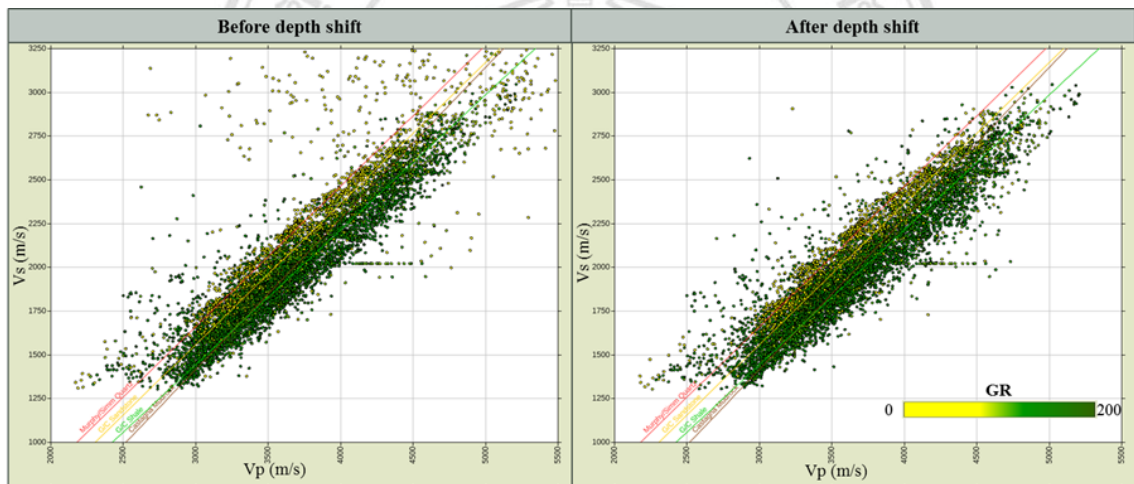


Figure 3.6 Vp vs. Vs cross-plot for Well-C, before depth shift (left) and after depth shift (right).

3.2 Shear Velocity Prediction

Measured shear-sonic log data were available in two of the four input wells, namely Well-B and Well-C. Shear velocity was predicted for Well-A and Well-D to optimize the geostatistical model used as input to the simulation and geostatistical inversion processes. A multi-linear regression (MLR) was used to predict shear velocity using other measured logs, such as compressional velocity (Vp), density (Rho), Gamma ray (GR), Neutron-porosity (NPHIE), and deep resistivity (AT90). The predicted Vs equation (3.1) was derived using logs with measured shear-sonic log data (Well-B and Well-C).

$$V_s = 165.4 + 0.58(V_p) - 136.83(\text{Rho}) - 0.735(\text{GR}) + 0.00482(\text{NPHIE}) + 253.98(\text{AT90}) \quad (3.1)$$

To verify the prediction, equation (3.1) was used to predict shear sonic velocity in Well-B and Well-C. The cross-plot between measured and predicted shear sonic velocity showed a good correlation of more than 90% (see Figure 3.7). Figure 3.8 compares predicted and measured shear-sonic velocity logs for Well-B and Well-C. The result showed a good agreement between the predicted and measured shear-sonic velocity logs.

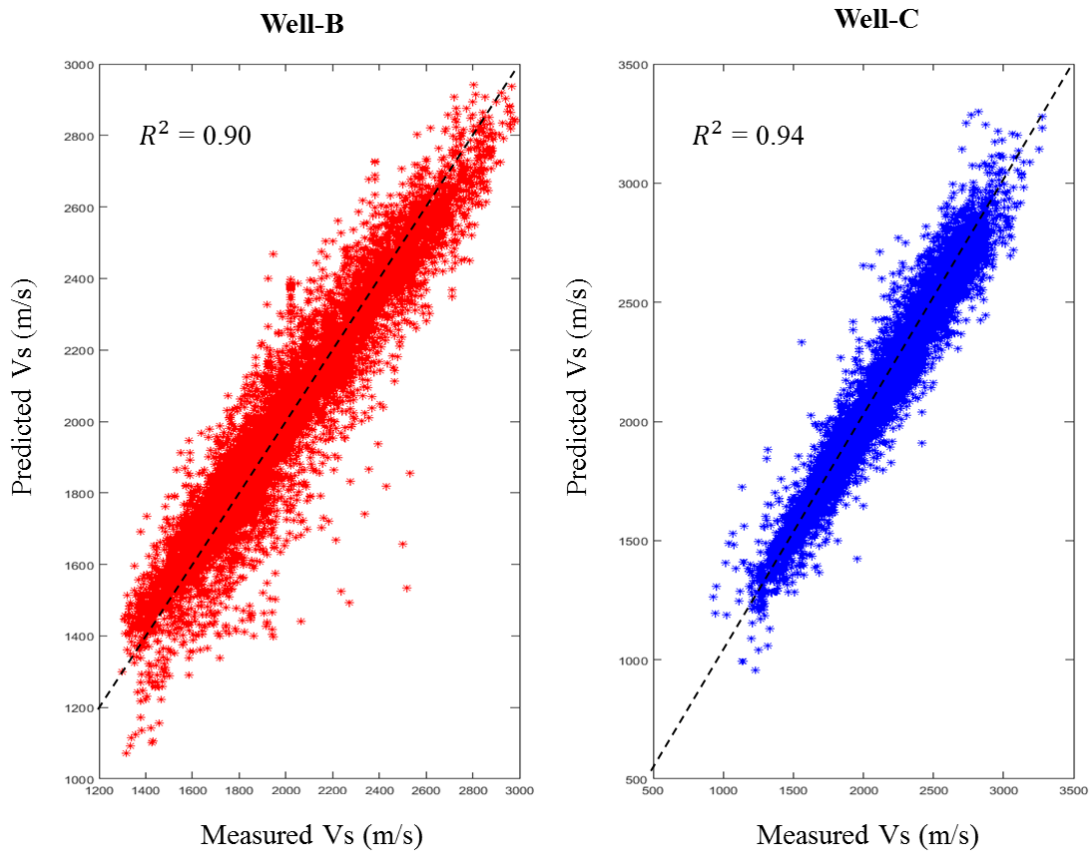


Figure 3.7 Cross-plot of measured vs. predicted shear-sonic velocity for Well-B and Well-C.

Copyright© by Chiang Mai University
All rights reserved

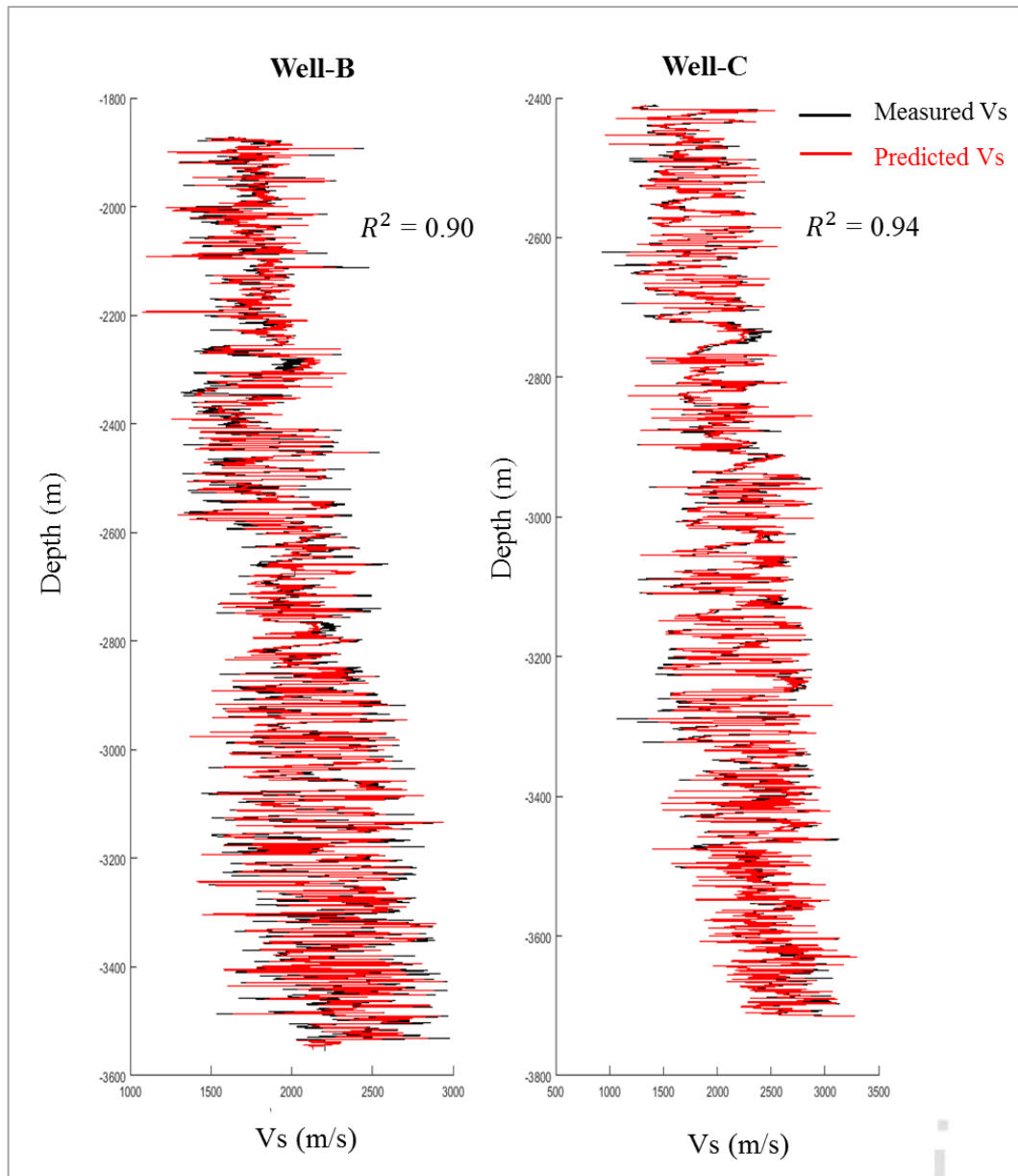


Figure 3.8 Comparison of measured shear-sonic velocity (black line) and predicted shear-sonic velocity (red line) for Well-B (left) and Well-C (right).

Consequently, shear-sonic velocity for Well-A and Well-D was predicted using equation (3.1). The predicted Vs log and the cross-plot between predicted Vs and measured Vp for Well-A and Well-D are shown in Figures 3.9 and 3.10. The cross-plots showed reliable trends of sand and shale as they followed the empirical trends derived from Well-B and Well-C.

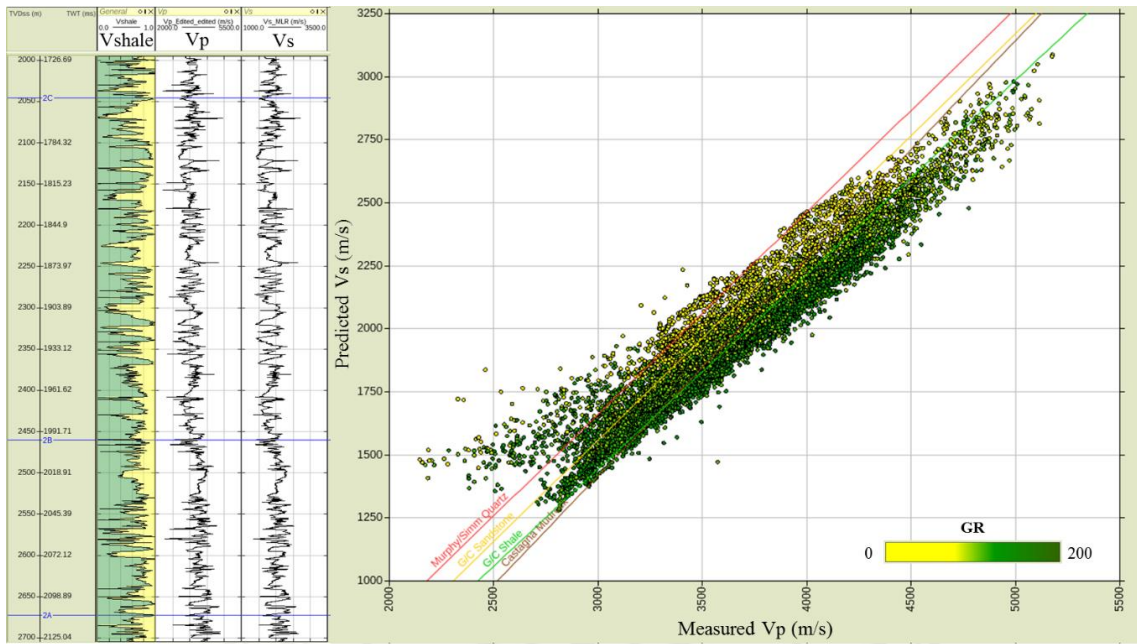


Figure 3.9 Predicted Vs for Well-A and cross-plot of measured Vp *versus* predicted Vs.

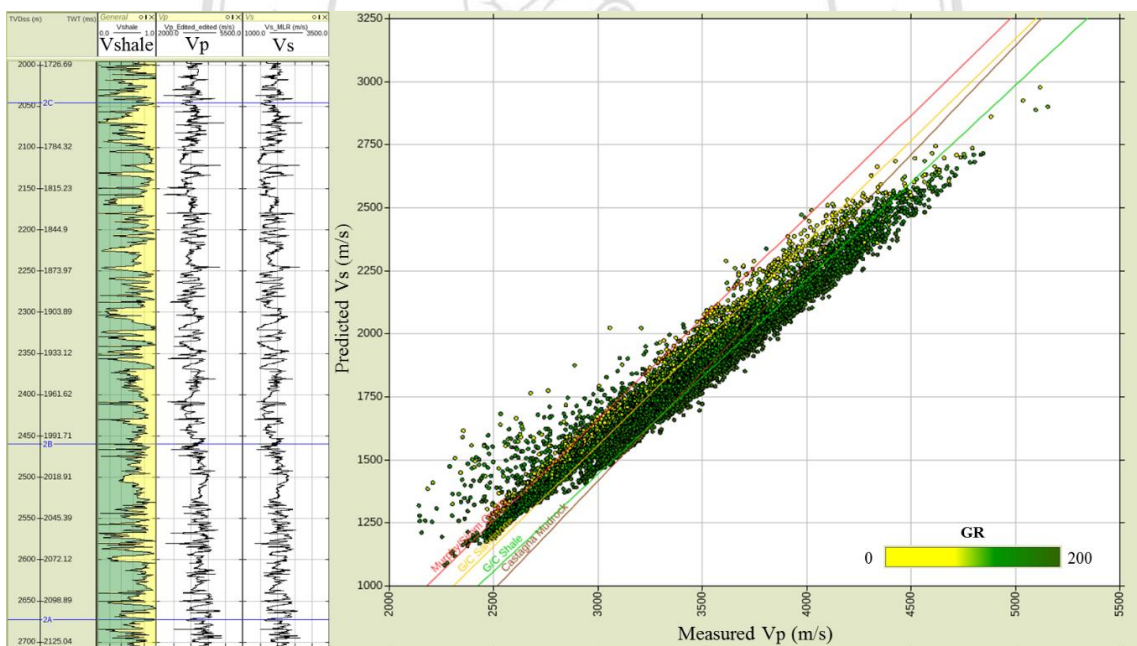


Figure 3.10 Predicted Vs for Well-D and cross-plot of measured Vp *versus* predicted Vs.

3.3 Rock-Physics Analysis

Rock-physics analysis was carried out to support lithology classification using elastic properties, such as P-impedance (AI), V_p/V_s , and density. The main objective was to define an appropriate lithology set (discrete properties) in relation to the stratigraphic interval of interest (H30 to H44), considered for this geostatistical inversion project.

AI, V_p/V_s , and density were cross-plotted using four input wells (Well-A, -B, -C and -D). Figure 3.11 shows the matrix cross-plot of the three elastic properties and their histograms, color-coded by lithology. All sands and shales were overlapping in the AI histogram. However, shales might be distinguished from sands when considering the V_p/V_s and mostly by density histograms.

In the matrix cross-plot, sand and shale showed a good separation in all cross-plot domains. However, discriminating gas sand from brine sand would be very challenging in this area, as there was a significant overlap of the elastic properties of gas and brine sand reservoirs. Fluid sensitivity was therefore not considered as part of the study, and all sands were therefore classified as one facies type. In addition, both histograms and cross-plots indicated that the properties of coal were widely scattered for all properties. However, low AI and low density values were still deemed to adequately classify coal. Based on these observations, three lithology types were selected as the final discrete property sets to be used for geostatistical model fitting and inversion (see Figure 3.12). The three lithology types are summarized in Table 3.1.

Table 3.1 Summary of lithology types for final discrete property set.

Lithology Types	Lithology Code	Description
Shale	0	Shale and tight sand
Sand	1	Water sand, gas sand and possible gas sand
Coal	2	Coal

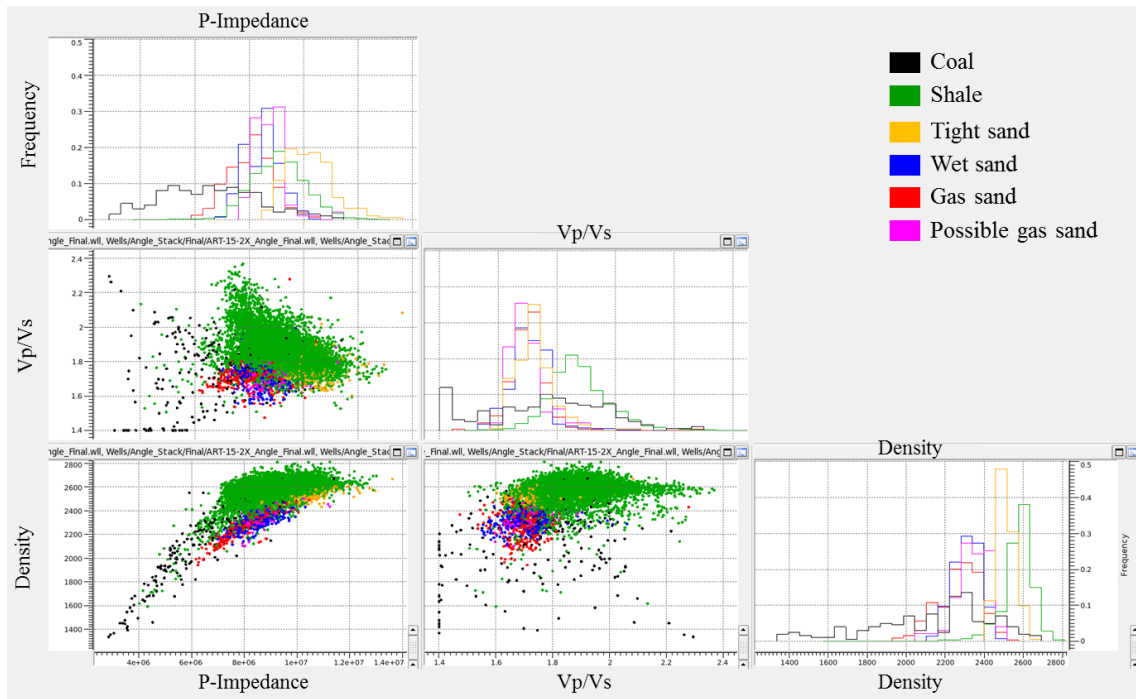


Figure 3.11 Matrix cross-plot of elastic properties, color-coded by original lithology types.

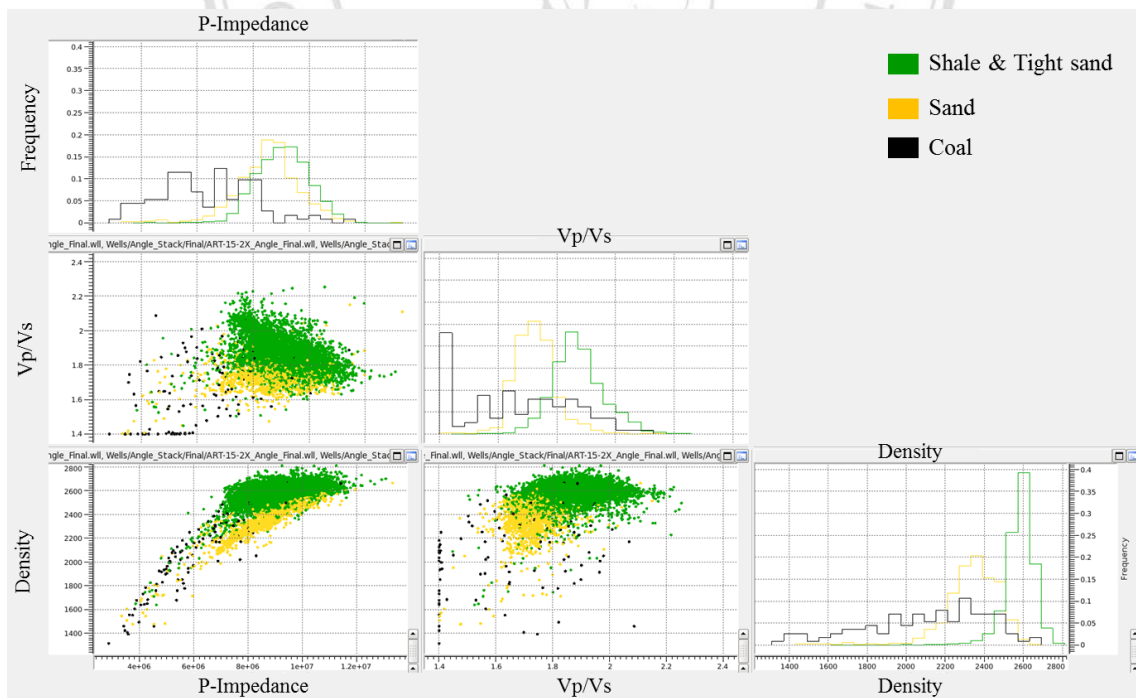


Figure 3.12 Matrix cross-plot of elastic properties, color-coded by the final lithology types to be considered in this study.

3.4 Seismic-to-Well Tie and Wavelet Extraction

Seismic data were tied to wells for all input wells, using Jason software (Well editor module). The check-shot data was used as the initial time-depth relationship, and was further calibrated using a combination of static time shifts and minor stretch/squeeze to optimize the match of the synthetic trace to the seismic trace. In this study, three of four wells (Well-A, -B and -D) had raw check-shot data available. Therefore, the seismic-to-well tie of Well-C used a time:depth relationship from Well-B, as these wells were located in the same structural trend and similar stratigraphy.

The polarity of the input seismic data was reverse polarity of zero-phase (“European standard”). An increase in acoustic impedance was represented by a trough or negative value. Figure 3.13 shows the seabed reflector represented by red color (a negative value) or trough in a wiggle display.

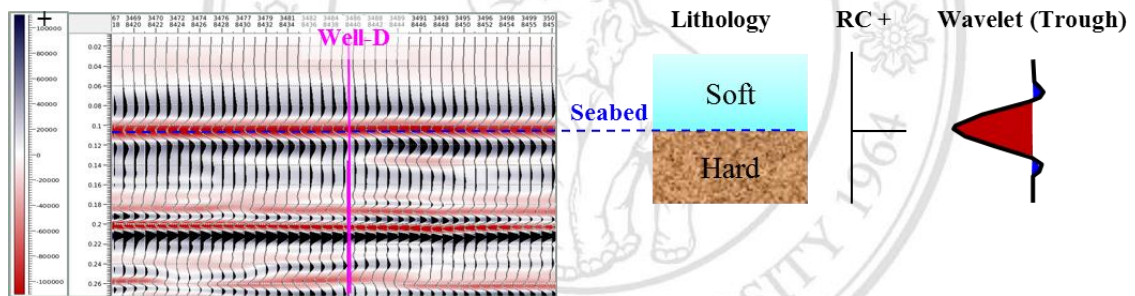


Figure 3.13 Wavelet polarity convention of the seismic input data, in this case reverse polarity (“European polarity”).

The input wavelets used for geostatistical inversion consisted of average wavelets that were calculated using 4 wells for each angle stack. The wavelet for each angle stack was extracted for all input wells based on its updated time:depth relationship. At each well location, wavelets were extracted for each angle stack within the same window (H20 to H50) and with the same wavelet length (120 ms). The extracted wavelet from each well was assessed for quality such as wavelet shape, frequency content, amplitude and phase spectra. Wells that provided good-quality wavelets were used as input to multi-well wavelet estimation for each angle stack, resulting in one wavelet per angle stack.

Figure 3.14 shows the extracted angle-dependent wavelets for each input well. Across all four angle stacks, three wells provided good quality wavelets that were used to create the multi-well wavelets, namely Well-A, -B and -D. Well-C was not included

for final wavelet calculation as it had relatively poor well-ties due to the bad seismic quality at this location. The multi-well wavelets of all angle stacks can be seen in Figure 3.15.

The final well ties used the multi-well wavelets for all angle stacks, and provided the final time:depth relationships for the seismic data at the respective well locations (Figure 3.20). The final well ties for Well-B are shown in Figures 3.16, 3.17, 3.18, and 3.19. Well-B tied best, probably due to the good seismic data quality in this area. Well-A and -D well ties were considered to be of moderate quality. Well-C provided very poor correlation because it was a deviated well drilled close to a fault plane, which affected the seismic data quality due to the fault shadow. A summary of the well ties using multi-well wavelets is in Table 3.2.

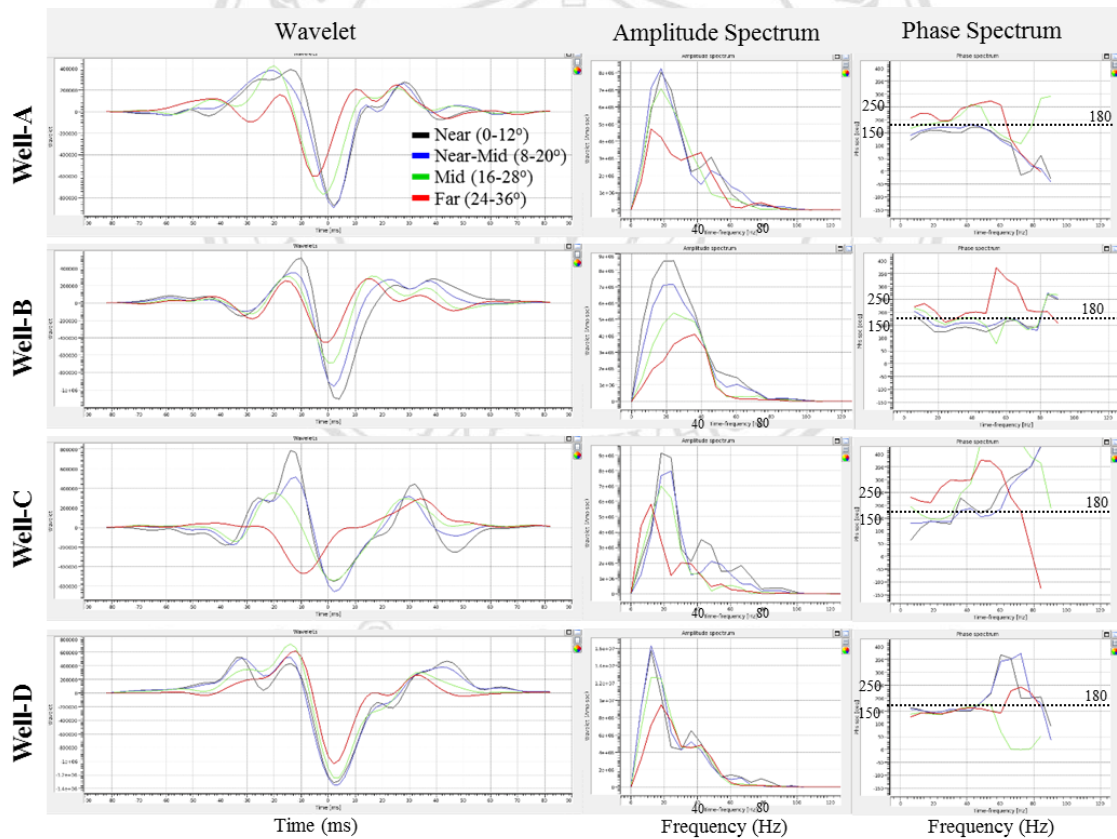


Figure 3.14 Wavelets extracted from each well, showing relatively stable wavelets at Well-A, -B and -D, while the extracted wavelets for Well-C were of poor quality.

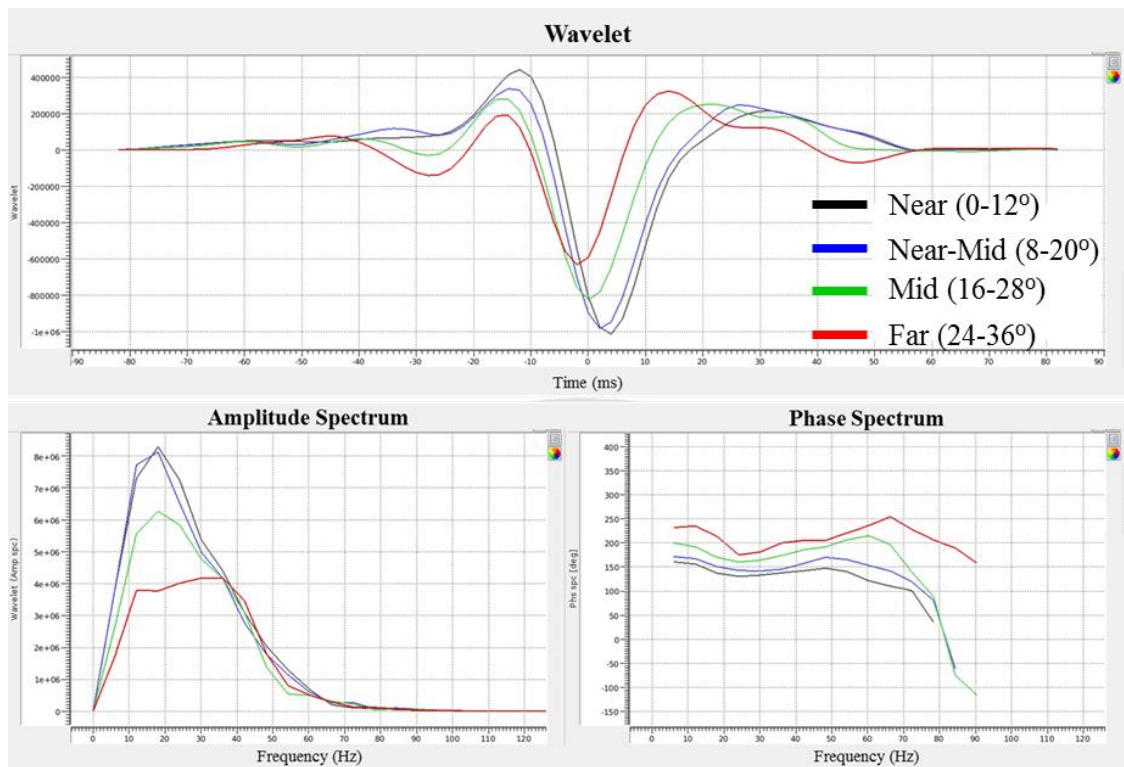


Figure 3.15 Multi-well wavelets for each angle stack, used as inputs to deterministic inversions.

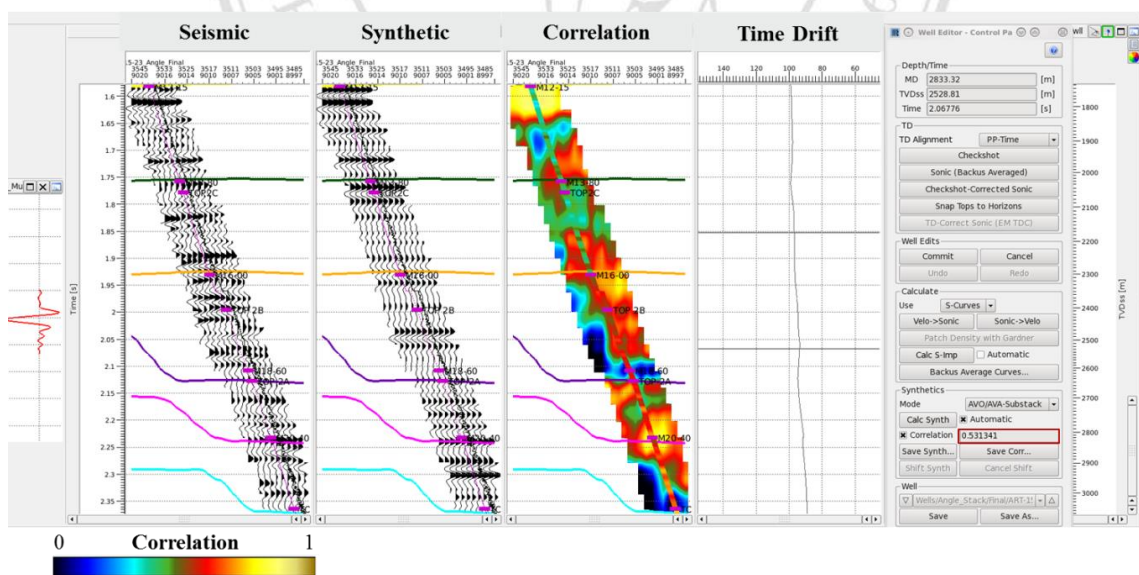


Figure 3.16 Well-to-seismic tie for Well-B showing the tie at the near angle stack (0-12°).

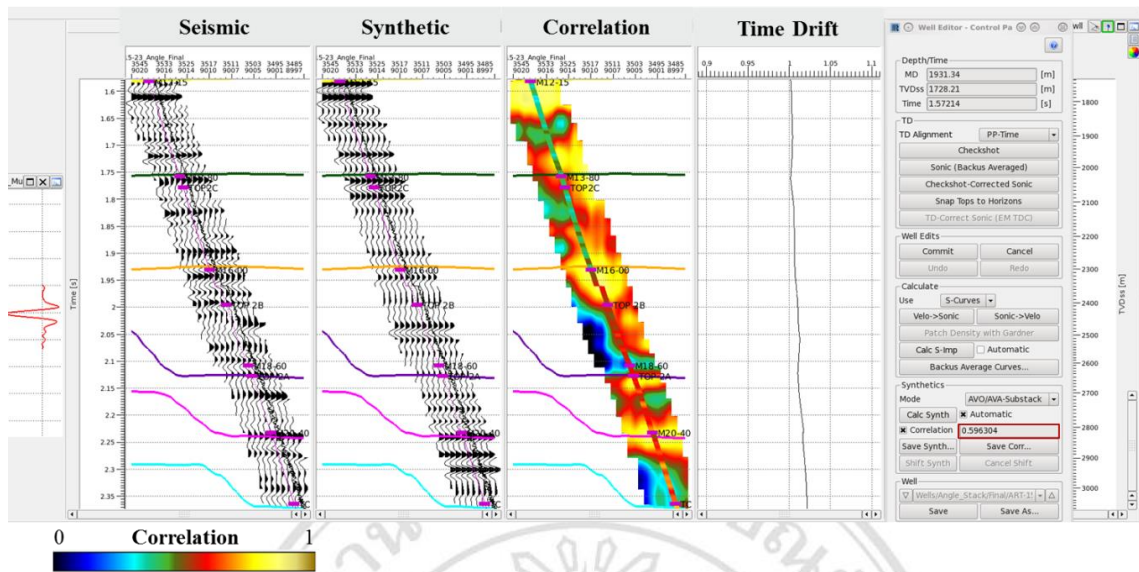


Figure 3.17 Well-to-seismic tie for Well-B showing the tie at the near-mid angle stack (8-20°).

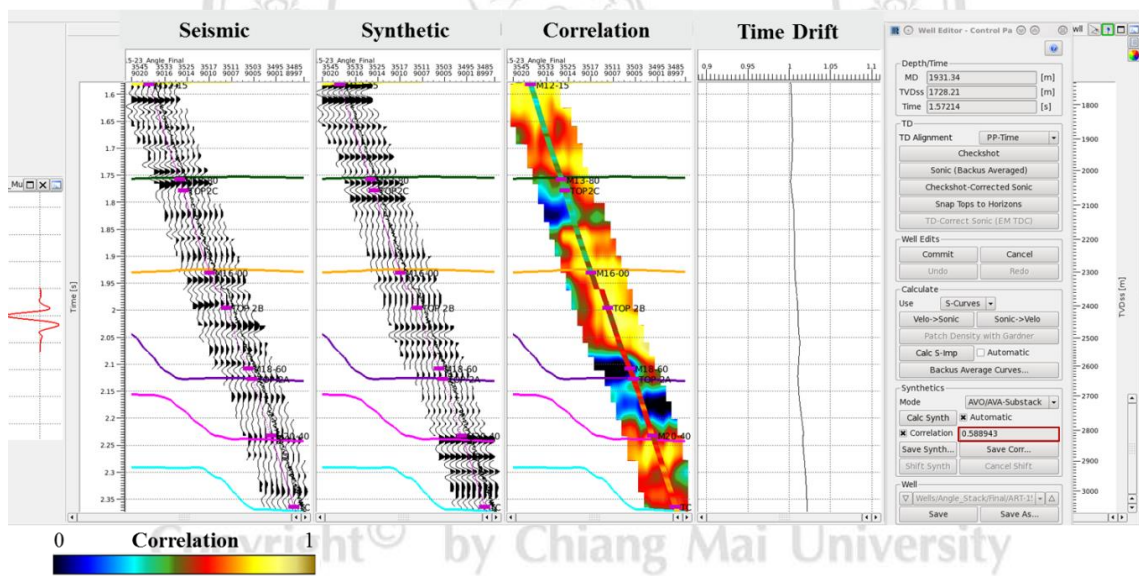


Figure 3.18 Well-to-seismic tie for Well-B showing the tie at the mid angle stack (16-28°).

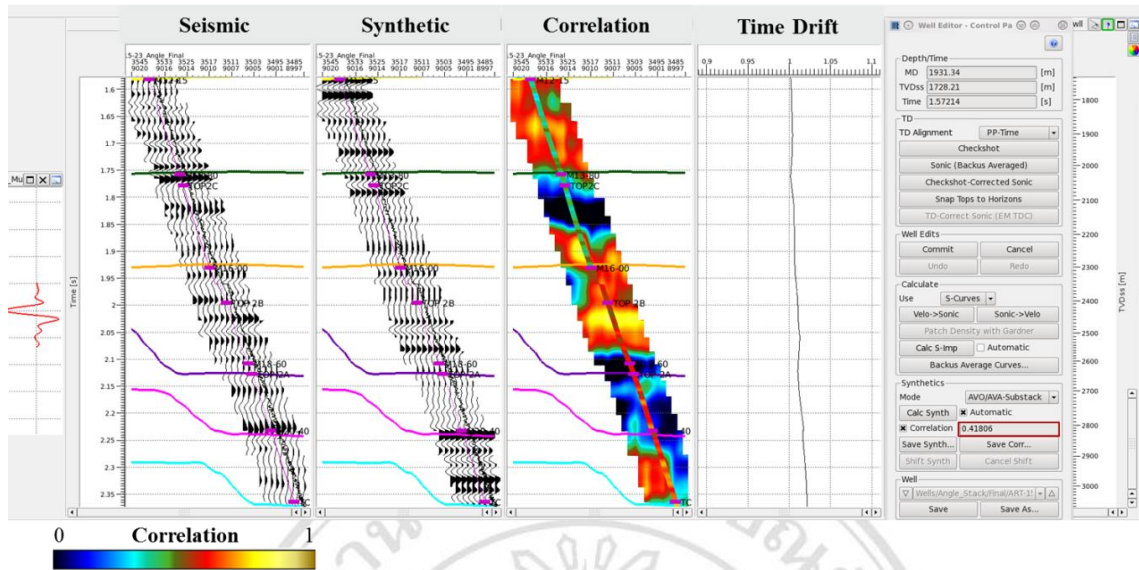


Figure 3.19 Well-to-seismic tie for Well-B showing the tie at the far angle stack (24-36°).

Table 3.2 Summary of the correlation coefficients at each well, using the final time-depth relationships.

Well	Angle Stacks			
	Near (0-12°)	Near-Mid (8-20°)	Mid (16-28°)	Far (24-36°)
Well-A	0.452	0.427	0.334	0.209
Well-B	0.531	0.596	0.588	0.417
Well-C	0.276	0.344	0.332	0.318
Well-D	0.331	0.400	0.389	0.230

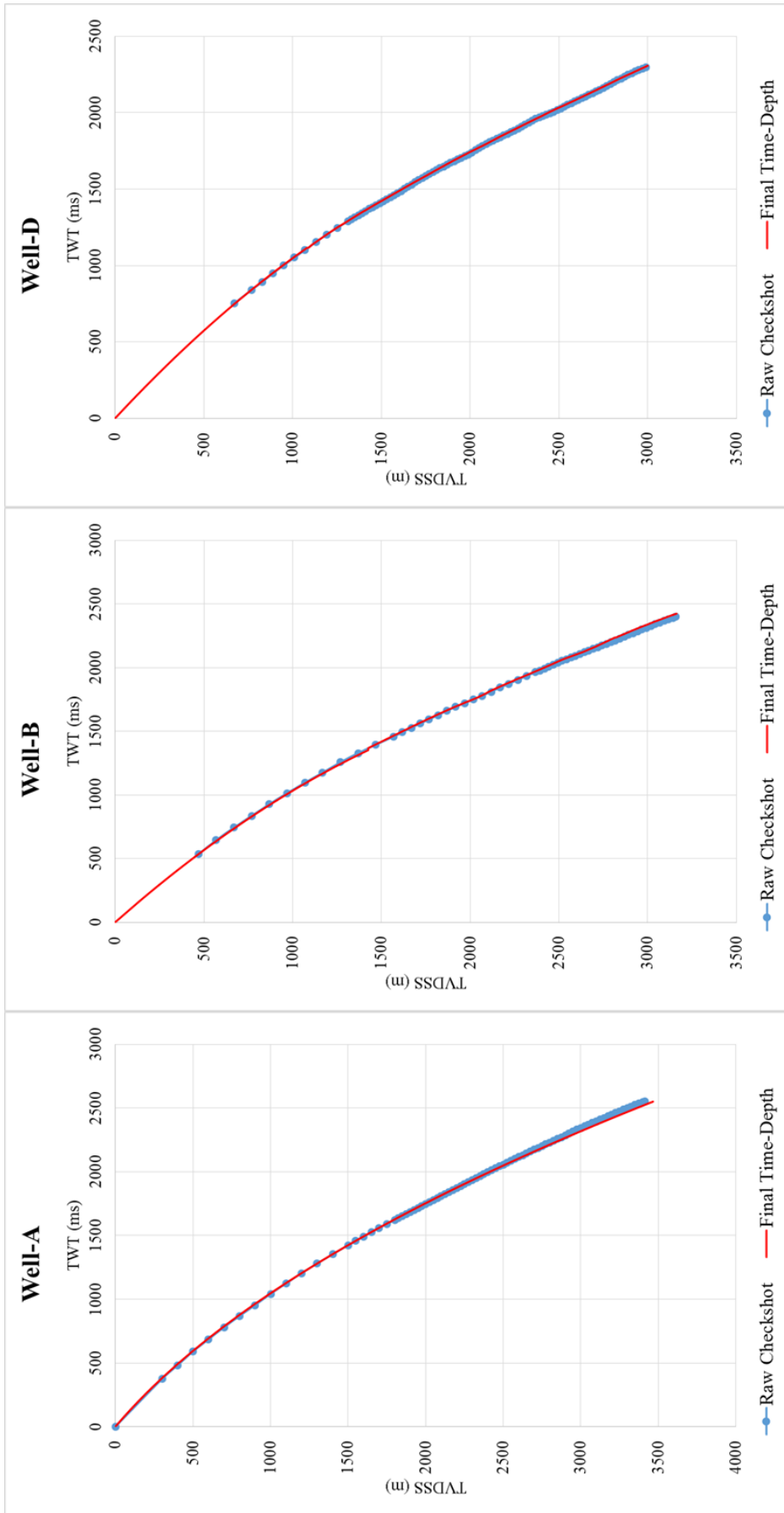


Figure 3.20 The comparison between original checkshot and final time:depth relationship of Well-A, Well-B and Well-D.